

# Arming Ru with Oxygen-Vacancy-Enriched RuO<sub>2</sub> Sub-Nanometer Skin Activates Superior Bifunctionality for pH-Universal Overall Water Splitting

Yapeng Li, Wentao Wang, Mingyu Cheng, Yafei Feng, Xiao Han, Qizhu Qian, Yin Zhu, and Genqiang Zhang\*

Water electrolysis has been expected to assimilate the renewable yet intermediate energy-derived electricity for green H<sub>2</sub> production. However, current benchmark anodic catalysts of Ir/Ru-based compounds suffer severely from poor dissolution resistance. Herein, an effective modification strategy is proposed by arming a sub-nanometer RuO<sub>2</sub> skin with abundant oxygen vacancies to the interconnected Ru clusters/carbon hybrid microsheet (denoted as Ru@V-RuO<sub>2</sub>/C HMS), which can not only inherit the high hydrogen evolution reaction (HER) activity of the Ru, but more importantly, activate the superior activity toward the oxygen evolution reaction (OER) in both acid and alkaline conditions. Outstandingly, it can achieve an ultralow overpotential of 176/201 mV for OER and 46/6 mV for the HER to reach 10 mA cm<sup>-2</sup> in acidic and alkaline solution, respectively. Inspiringly, the overall water splitting can be driven with an ultrasmall cell voltage of 1.467/1.437 V for 10 mA cm<sup>-2</sup> in 0.5 M H<sub>2</sub>SO<sub>4</sub>/1.0 M KOH, respectively. Density functional theory calculations reveal that armoring the oxygen-vacancy-enriched RuO<sub>2</sub> exoskeleton can cooperatively alter the interfacial electronic structure and make the adsorption behavior of hydrogen and oxygen intermediates much close to the ideal level, thus simultaneously speeding up the hydrogen evolution kinetics and decreasing the energy barrier of oxygen release.

## 1. Introduction

The goal of CO<sub>2</sub> neutralization leverages the exploitation of renewable energy,<sup>[1]</sup> while water electrolysis has been expected as a promising manner to store the clean but intermittent electricity from wind, solar, tide, and so on, into the chemical bond, thus could meet the diverse applications in the future H<sub>2</sub> economy.<sup>[2,3]</sup> However, the core electrocatalysts are still unsophisticated, which is mainly hindered by the kinetics-sluggish oxygen evolution reaction (OER) on the anode side.<sup>[4–6]</sup>

Although the earth-abundant, first row (3d) transition metal (oxy)hydroxides, and metal–organic frameworks (MOFs) have garnered intense interest for their encouraging activity, such as FeNi-LDH,<sup>[7]</sup> FeCoW oxyhydroxide,<sup>[8]</sup> (Ni<sub>2</sub>Co<sub>1</sub>)<sub>0.925</sub>Fe<sub>0.075</sub>-MOF-NF,<sup>[9]</sup> the active dissolvability and degradability in the acidic solution overshadow their competitiveness. On the other hand, hydrogen evolution reaction (HER) activity of the state-of-the-art Pt decreases to ≈2 to 3 orders of magnitude

in the alkaline media than that in the proton-rich environment (only needs (tens of) millivolts of overpotential to reach the current density of 10 mA cm<sup>-2</sup><sub>geo</sub>).<sup>[10]</sup> These pH-sensitive catalysts burden the integrated water electrolysis system, further stressing the necessity of developing stable electrocatalysts in the pH-universal condition.<sup>[11]</sup>

Metallic Ru-based compounds possess favorable binding energy with H, robust thermostability, good anticorrosion ability, as well as cost efficiency (about 1/5 price of Pt), thus have recently gained ever-increasing interest as pH-universal electrocatalysts for HER.<sup>[12]</sup> For example, Ru nanoparticles dispersed in nitrogenated holey 2D carbon structure (Ru@C<sub>2</sub>N) exhibit outstanding activity (13.5/17 mV@10 mA cm<sup>-2</sup> in 0.5 M H<sub>2</sub>SO<sub>4</sub>/1.0 M KOH) for HER.<sup>[13]</sup> Ideally, it is highly desired if functionalization can be exerted to endow Ru with promising catalytic activity for OER while simultaneously inheriting its HER capacity, which could be a kind of superior candidates for overall water splitting catalysts. Constructing core/shell configuration has been demonstrated as a powerful tactic, which can incorporate the strain and ligand effect to steer its adsorption/desorption kinetics with the

---

Y. Li, M. Cheng, Y. Feng, Q. Qian, Y. Zhu, G. Zhang  
 Hefei National Research Center for Physical Sciences at the Microscale  
 CAS Key Laboratory of Materials for Energy Conversion  
 Department of Materials Science and Engineering  
 University of Science and Technology of China  
 Hefei, Anhui 230026, P. R. China  
 E-mail: gqzhangmse@ustc.edu.cn

W. Wang  
 Guizhou Provincial Key Laboratory of Computational Nano-Material Science  
 Guizhou Education University  
 Guiyang 550018, P. R. China

X. Han  
 Center of Advanced Nanocatalysis (CAN)  
 Department of Applied Chemistry  
 University of Science and Technology of China  
 Hefei, Anhui 230026, P. R. China

 The ORCID identification number(s) for the author(s) of this article can be found under <https://doi.org/10.1002/adma.202206351>

DOI: 10.1002/adma.202206351

intermediates for optimizing the activity.<sup>[14,15]</sup> For example, Qiao et al. have successfully armed the Ru core with the acid/alkaline-stable IrO<sub>x</sub> skin (Ru@IrO<sub>x</sub>), the charge redistribution and strain effect induced by the highly strained ruthenium core and the partially oxidized iridium shell across the metal-metal oxide heterojunction enhance the OER activity ( $\eta_{10} = 282$  mV) and stability (90% retentivity@24 h).<sup>[16]</sup> However, the interfacial electronic redistribution and strain effect activated by the core-shell heterostructure are short-range,<sup>[17]</sup> which means the sub-nanometer skin with several atomic layers is essential to exert the synergistic effect, thus imposing stringent constraints on the delicate assembly of the ultrathin armor via facile yet better methods. Besides, digging out the water electrolysis potentiality of the Ru-based materials as much as possible, especially improving its usability and buffering capacity in the pH-wide range is of much necessary to increase the material's survivability in the practical working conditions.

Herein, we present a functionalization strategy by arming Ru nanoclusters with sub-nanometer RuO<sub>2</sub> skin enriched with oxygen vacancy (O<sub>v</sub>), that can activate the superior OER catalytic activity, and simultaneously inherit the HER performance, thus achieving the impressive catalytic activity with the ultra-small overpotentials of 176 and 201 mV at 10 mA cm<sup>-2</sup> for OER in acidic and alkaline solution, also possessing the superior HER performance (47 mV@10 mA cm<sup>-2</sup> in 0.5 M H<sub>2</sub>SO<sub>4</sub>; 6 mV@10 mA cm<sup>-2</sup> in 1.0 M KOH). Theoretical calculation discloses that strengthening the Ru with O<sub>v</sub> enriched RuO<sub>2</sub> can optimize the electronic structure to make a more thermoneutral H adsorption/desorption for HER and reduce the energy barrier toward OER. Therefore, the Ru@V-RuO<sub>2</sub>/C HMS integrates and enlarges the respective advantages of the HER/OER active components for expressing the extraordinary bifunctionality toward water electrolysis, which only needs the low working voltage of 1.467/1.437 V in 0.5 M H<sub>2</sub>SO<sub>4</sub>/1.0 M KOH to reach 10 mA cm<sup>-2</sup>, consequently realizing the obvious H<sub>2</sub> generation driving by one AA battery.

## 2. Results and Discussion

The synthetic procedures are cost-effective and scalable, as illustrated in **Figure 1a**, including the formation of Ru/C hybrid microsheet via thermal annealing of Ru<sup>3+</sup>-melamine precursor in inert gas, followed by covering O<sub>v</sub> enriched RuO<sub>2</sub> sub-nanometer skin on Ru surface to obtain the final product. Specifically, the precursor of Ru<sup>3+</sup>-melamine (Figure S1, Supporting Information) can be formed via the electrostatic interaction between the N atom in the melamine molecule and the Ru<sup>3+</sup> ion. Then, the carbothermal reduction forms the carbon-based hybrid microsheet decorated with the dense Ru nanoclusters (denoted as Ru/C HMS, Figure S2, Supporting Information) owing to the “self-templating” of melamine crystal.<sup>[18]</sup> Then, low-temperature oxidation in the air can skillfully arm the sub-nanometer skin of RuO<sub>2</sub> for the Ru core. The morphology (Figure 1b and Figure S3, Supporting Information) of the final product inherits the original sheet-like morphology decorated with lots of tiny nanoclusters. The enlarged transmission electron microscopy (TEM) image (Figure 1c) displays that uniform clusters centered at 4.9 nm (Figure S4, Supporting Information) distribute on the matrix orderly, which balances the high density and good dispersion. Be-

sides, the X-ray diffraction (XRD) pattern (Upper in Figure 1d) reflects the existence of RuO<sub>2</sub> (PDF#43-1027) and Ru (PDF#70-0274). The Raman spectrum (Bottom in Figure 1d) contains the classical signals of the D band and G band, supporting the conservation of carbon. The Brunauer–Emmett–Teller (BET) analysis suggests the surface area of this microsheet is as high as 193 m<sup>2</sup> g<sup>-1</sup>, along with a large number of mesopores concentrated at 3 nm (Figure S5, Supporting Information), which is easier for the free diffusion of oxygen and hydrogen gas molecules.<sup>[19]</sup> The aberration-corrected high-angle annular dark-field scanning transmission electron microscopy (HAADF-STEM) image in Figure 1e presents that the core-shell clusters widely exist in the porous microsheet. Some nanopores are visual from the microsheet, coinciding with the BET result. Notably, the existence of graphitic carbon marked with the yellow arrow in Figure 1f and Figure S6, Supporting Information supports the above Raman analysis, which may serve as the electron reservoir for providing electrons to the Ru-based constitute, thus can intensify its anticorrosion ability and relieves its overoxidation for improving the stability.<sup>[20]</sup> Its role in the hybrid will be discussed later. The aberration corrected HAADF-STEM analysis portrayed in Figure 1g display a clear core-shell nanostructure with the different Z-contrast. To know the precise composition of the core-shell nanostructure, two different regions containing core and shell were analyzed in detail. As shown in Figure 1h,i, the inner core with the interplanar distances (d-space) of 2.17 and 2.08 Å can be indexed as the (002) and (101) planes of hexagonal Ru phase, while the outer shell with the d-space of 3.15 and 2.50 Å belong to the (110) and (101) planes of tetragonal RuO<sub>2</sub> phase, demonstrating that the inner core of Ru has been clothed with several atomic layers RuO<sub>2</sub> shell. The sub-nanometer skin can not only protect the Ru core for avoiding overoxidation but also change the interface strain and receive the electronic regulation from the inner core to boost the reactivities efficiently. Strikingly, the inverted fast Fourier transform images (Figures S7, Supporting Information) present the distorted atomic arrangement in the inner core and the broken atomic arrangement integrity in the outer shell, implying the possible existence of strain effect at the core-shell interface.<sup>[21,22]</sup> This phenomenon widely exists in this kind of core-shell structure (Figure S8, Supporting Information). Visually, the geometric phase analysis (GPA) showcases the asymmetrical distribution of strains centered at the interface of the Ru and RuO<sub>2</sub> microregion (Figure 1j), indicating the existence of the strong strain effect in this core@shell heterostructure, which may be beneficial to optimize the kinetics and expose more extra active sites.<sup>[23,24]</sup> Besides, the low-magnification HAADF-STEM image and the corresponding elemental mapping results (Figure S9, Supporting Information) portray the uniform presence of C, N, Ru, and O elements in this composite. Next, the complexity and subtlety of arming the sub-nanometer skin for the core to form the metal@metal oxide heterostructure have been discerned carefully by altering the oxidation temperature. At 150 °C, the oxygen almost cannot combine with Ru to form the corresponding oxide (Figure S10, Supporting Information), and the nanoparticles with nearly unchanged size disperse on the mainland uniformly (Figure S11, Supporting Information). At the higher temperature of 250 °C, only the cracked microsheet decorated with slightly aggregated oxides can be obtained. Thus, the temperature of 200 °C is critical to precisely arm the

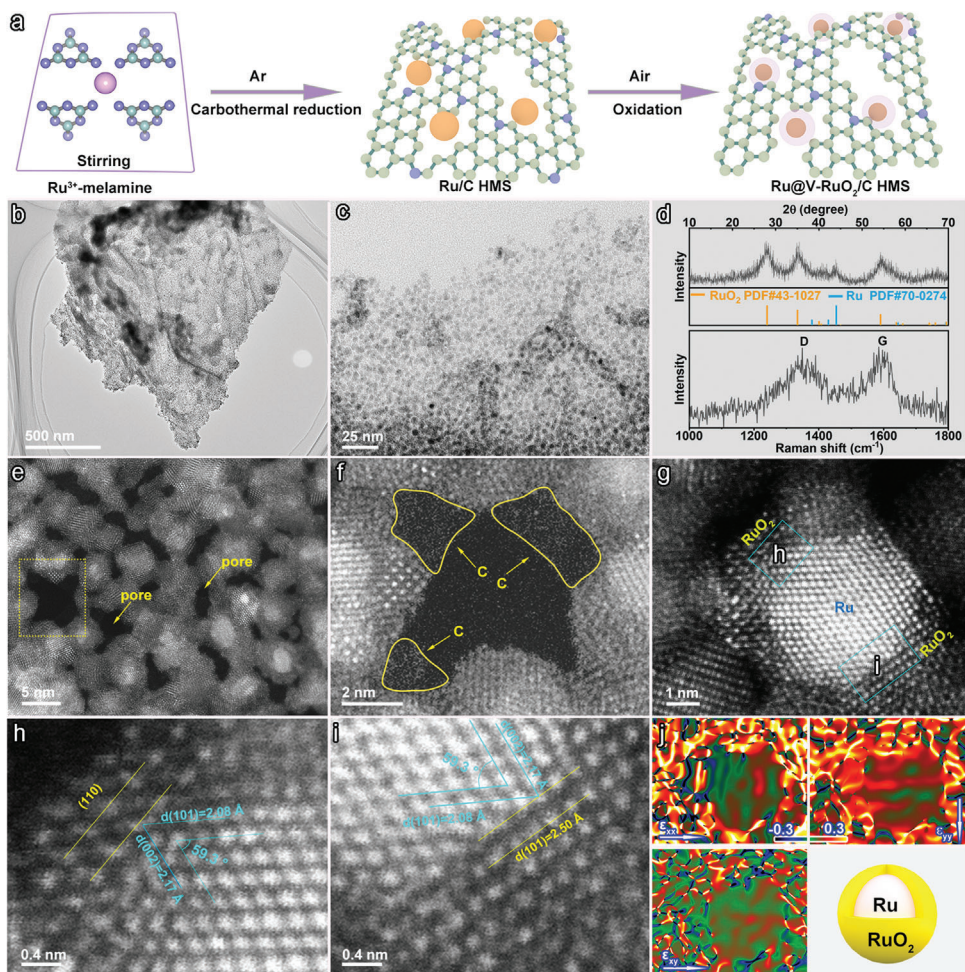


**Figure 1.** The synthetic process and structural characterizations for Ru@V-RuO<sub>2</sub>/C HMS. a) Schematic illustration of the formation; b) plan view and c) high-magnification TEM images; d) XRD pattern and Raman spectrum; e–i) aberration-corrected HAADF-STEM; and j) the corresponding strain maps along  $\epsilon_{xx}$ ,  $\epsilon_{yy}$ ,  $\epsilon_{xy}$  processed by the GPA algorithm, as well as the core–shell model; positive and negative values in the gradational bar represent the tensile and compressive strains, respectively.

sub-nanometre RuO<sub>2</sub> skin for the Ru core, and the structural information will be discussed in the following.

X-ray photoelectron spectroscopy (XPS) is conducted to study the chemical states of Ru@V-RuO<sub>2</sub>/C HMS. As depicted in Figure 2a, the Ru 3d<sub>5/2</sub> binding energy of the prepared Ru@V-RuO<sub>2</sub>/C HMS (280.7 eV) locates in the middle of Ru/C HMS (280.1 eV) and RuO<sub>2</sub> (280.9 eV), implying the surface valence of Ru is less than +4, which is of very significance for effectively suppresses the overoxidation of Ru<sup>4+</sup>, thus contributing to the high catalytic stability.<sup>[25]</sup> Furthermore, the deconvoluted O 2p peaks (Figure S12, Supporting Information) of Ru@V-RuO<sub>2</sub>/C HMS located at 529.3 eV, 530.6 eV, 531.2 eV, and 533.4 eV can be attributed to the lattice O (oxide) arising from the Ru—O, the OH ions (OH) that integrated into the outer surface, the oxygen vacancy (O<sub>v</sub>), and the adsorbed water molecule (H<sub>2</sub>O<sub>ad</sub>).<sup>[26]</sup> Subsequently, the XPS survey spectra provided in Figure S13, Supporting Information, displayed the stable elemental species while the variable elemental ratio of these samples oxidized at different temperatures. Owning to the partial overlap of C 1s and Ru 3d<sub>5/2</sub>, the diacritical N 1s signal inserted in Figure S13a, Supporting In-

formation verified the existence of carbon during the oxidation process, which coincides with the above Raman results. As depicted in Figure S13b,c, Supporting Information, the binding energy of the Ru 3d and 3p peaks of the samples obtained at 200 °C falls between those of the samples oxidized at 150 °C and 250 °C. In particular, the low-temperature product synthesized at 150 °C still shows the characteristic peaks of Ru metal. Meanwhile, the O 1s fine-scanning spectra disclose the attenuation of existing oxygen vacancy when oxidizing the product at 250 °C compared with that oxidized at 200 °C, supported by the inserted electron paramagnetic resonance (EPR) spectrum, thus this product is named RuO<sub>2</sub>/C microsheet (RuO<sub>2</sub>/C MS). While the O 1s profile of the low-temperature sample (150 °C) like the twin of the above Ru/C MS (Figure S12, Supporting Information), excepts the marginally enlarged OH section, indicating the increased oxygen content in the Ru-based microsheet oxidized at 150 °C, hence this sample was denoted as O-Ru/C hybrid microsheet (O-Ru/C HMS). Further, to gain the variation of element compositions and chemical states of this core–shell composite, the XPS depth profile was further analyzed (see Note S1, Supporting Information for

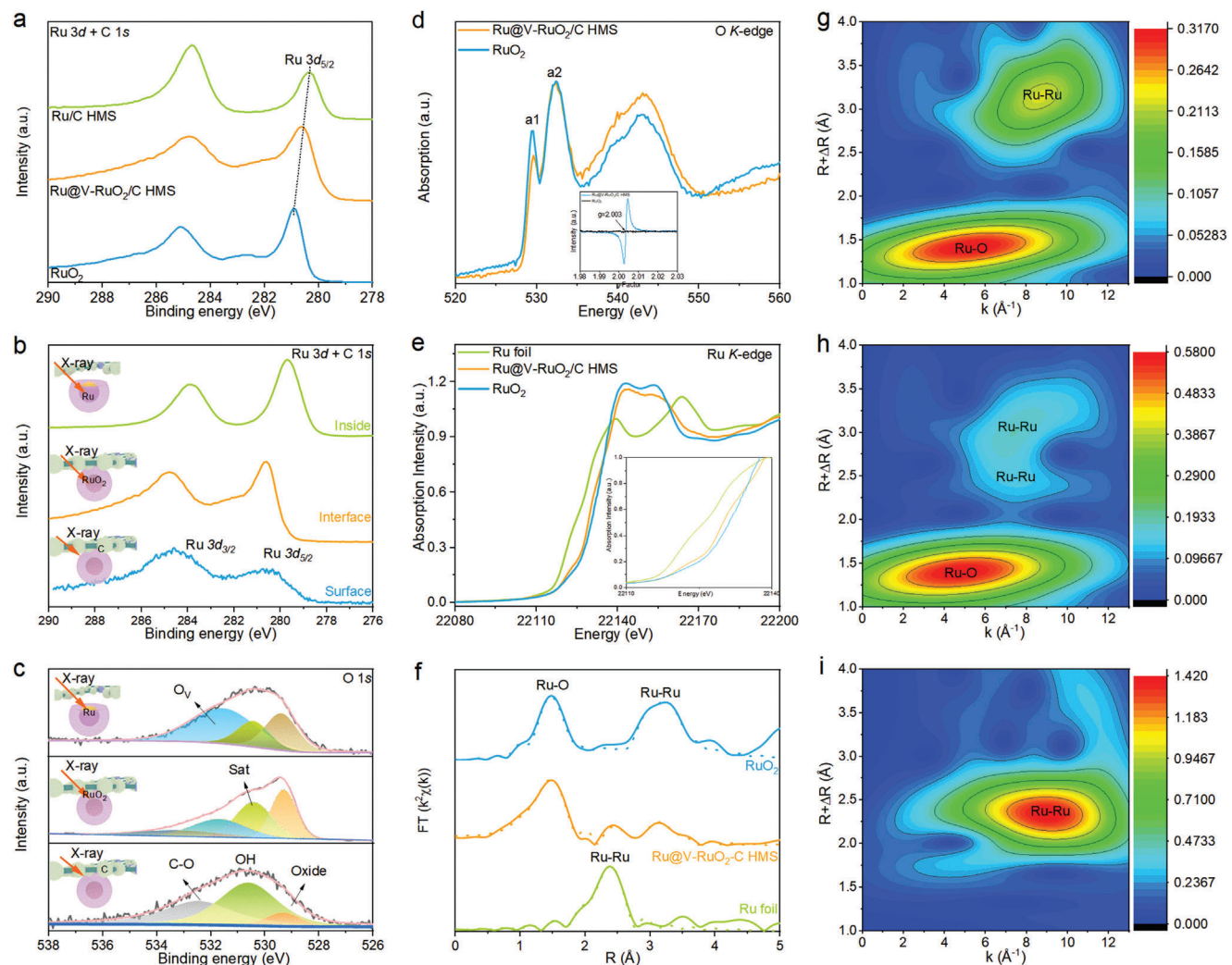


**Figure 2.** The fine structure analysis of Ru@V-RuO<sub>2</sub>/C HMS. a) The Ru 3d + C 1s high-resolution spectra of Ru/C HMS, Ru@V-RuO<sub>2</sub>/C HMS, and RuO<sub>2</sub>; b,c) the Ru 3d + C 1s (b) and O 1s (c) high-resolution spectra of Ru@V-RuO<sub>2</sub>/C HMS at different depths; the inset shows the EPR spectra of them; d) the normalized O K-edge spectra of Ru@V-RuO<sub>2</sub>/C HMS and RuO<sub>2</sub>; e) the normalized Ru K-edge spectra and f) FT-EXAFS spectra (line: raw data, scatter: fitting) of Ru@V-RuO<sub>2</sub>/C HMS, Ru foil, and RuO<sub>2</sub>; g–i) WT of the Ru K-edge EXAFS contour plots of RuO<sub>2</sub> (g), Ru@V-RuO<sub>2</sub>/C HMS (h), and Ru foil (i).

details). As shown in the survey profile (Figure S14, Supporting Information), from the surface to the interface and then to the inside, the relative intensity of Ru strength gradually along with the attenuation of C 1s and O 1s peaks, underscoring the inhomogeneity of the as-resultant sample. Especially, the strengthening and negative shift of Ru 3d<sub>5/2</sub> peaks (Figure 2b) suggests the relatively increasing content of metallic Ru, supporting the formation of metal@metal oxide heterostructure.<sup>[27]</sup> The binding energy of core Ru metal is  $\approx 0.1$  eV higher than that of Ru/C HMS, means the possible interfacial charge transfer from the core to the shell, thus may further suppress the overoxidation of the RuO<sub>2</sub> during the OER process.<sup>[28]</sup> The depth O 1s fine-scanning signal (Figure 2c) displays the relative increase of O<sub>v</sub> (531.2 eV) in the interface of Ru and RuO<sub>2</sub>, which may endow this hybrid with excellent electrocatalytic performance.<sup>[29]</sup>

To further evaluate the hybridization of Ru—O bands, the O K-edge X-ray absorption spectroscopy (XAS) has been performed.

The two sharp features at 529.6 and 532.3 eV denoted as a1 and a2 represent the unoccupied orbitals of O 2p hybridized with Ru 4d t<sub>2g</sub> and e<sub>g</sub> states, and the broad peaks range from 535 to 550 eV are assigned to the excitation of core electrons into O 2p and Ru 5sp hybridized states.<sup>[30]</sup> The small a1 peak intensity normalized by the adsorption background than that of RuO<sub>2</sub> reference implies the less hybridization of Ru—O bonds and the weaker binding strength, which may be caused by the existence of oxygen vacancy of our sample than the commercial RuO<sub>2</sub>.<sup>[31]</sup>

Moreover, the Ru K-edge X-ray absorption near-edge structure (XANES) and extended X-ray absorption fine structure (EXAFS) measurements were executed to analyze the electronic structure. As shown in Figure 2e, the XANES spectrum of Ru@V-RuO<sub>2</sub>/C HMS shifts to positive energy than that of the Ru foil reference, while slightly moving to lower energy than that of the RuO<sub>2</sub>, implying the average oxidation state of the Ru species in Ru@V-RuO<sub>2</sub>/C HMS is close but less than +4, matched well with the

XPS results. Furthermore, the chemical identities can be revealed from the Fourier transform of the  $\kappa^2$ -weight EXAFS (FT-EXAFS, Figure 2f and Table S1, Supporting Information). The Ru foil reference possesses the main peak of Ru–Ru interaction at  $\approx 2.4 \text{ \AA}$ , and commercial RuO<sub>2</sub> exhibits two peaks associating with the first shell of the Ru–O bond ( $\approx 1.5 \text{ \AA}$ ) and the second-shell Ru–Ru bond ( $\approx 3.2 \text{ \AA}$ ). As expected, Ru@V-RuO<sub>2</sub>/C HMS displays three types of peaks, including the slightly constrict Ru–O (1.96  $\text{\AA}$ ) and Ru–Ru (3.55  $\text{\AA}$ ) bond length than those of RuO<sub>2</sub> (1.97  $\text{\AA}$  and 3.56  $\text{\AA}$ , respectively), as well as the extended Ru–Ru bond (from 2.67  $\text{\AA}$  to 2.78  $\text{\AA}$ ) belong to the Ru core, indicating the strong strain effect between the inner Ru and the outer RuO<sub>2</sub> skin. Besides, the smaller average coordination number (N) of Ru–O in the Ru@V-RuO<sub>2</sub>/C HMS (5.7) than that of RuO<sub>2</sub> (6) underpins the existence of O<sub>v</sub>, which can expose abundant coordination-unsaturated sites and increase the conductivity for accelerating the electrocatalytic process. Next, three special regions can be visualized from the wavelet transform (WT) of Ru K-edge EXAFS oscillations of Ru@V-RuO<sub>2</sub>/C HMS (Figure 2h), assigned to the upper RuO<sub>2</sub> (Figure 2g) and the bottom Ru foil (Figure 2i), respectively, in line with the corresponding curve-fitting curves in Figure 2f. Explicitly, the core@shell Ru@RuO<sub>2</sub> with the O<sub>v</sub> has been formed, and its relationship with the electrocatalytic behavior will be studied and discussed below.

The electrocatalytic activity was extensively characterized using a standard three-electrode system with a graphite rod as the counter electrode and Ag/AgCl (Saturated KCl) or Hg/HgO (1.0 M KOH) as the reference electrode. First, a series of electrochemical test results (Figures S15–S20, Supporting Information) shows that the Ru@V-RuO<sub>2</sub> hybrid microsheet synthesized at 200 °C has the optimized bifunctionality toward OER and HER than those of O-Ru/C HMS (150 °C) and RuO<sub>2</sub>/C HMS (250 °C), hence its comparison with the benchmarking catalysts, such as commercial RuO<sub>2</sub> and Pt/C, will be performed below.

The IR-compensated polarization curves (Figure 3a) display that Ru@V-RuO<sub>2</sub>/C HMS has the best performance than that of commercial RuO<sub>2</sub> and synthesized Ru/C HMS in 0.5 M H<sub>2</sub>SO<sub>4</sub>. Concretely, to reach the geometric current density of 10 mA cm<sup>-2</sup>, it exhibits the impressively low overpotential ( $\eta_{10}$ ) of 176, 101 mV smaller than that of commercial RuO<sub>2</sub> (Figure S21, Supporting Information). In 1.0 M KOH, Ru@V-RuO<sub>2</sub>/C HMS still keeps its supremacy (Figure 3b), and  $\eta_{10}$  is as low as 201 mV, which is almost 70% of the commercial RuO<sub>2</sub>. Noticeably, the feeble rise of Ru/C HMS reflects its poor reaction kinetics, mainly owing to the oxidation and dissolution of Ru species during the OER process.<sup>[32]</sup> Meanwhile, the smaller Tafel slope values ( $b$ ) of Ru@V-RuO<sub>2</sub>/C HMS in both acid (45.6 mV dec<sup>-1</sup>, Insets in Figure 3a) and alkaline (44.8 mV dec<sup>-1</sup>, Insets in Figure 3b) environments than those of RuO<sub>2</sub> (104.9 and 114.3 mV dec<sup>-1</sup>, respectively) explain its splendid OER performance. Remarkably, comparing the  $\eta_{10}$  and  $b$  of Ru@V-RuO<sub>2</sub>/C HMS with the reported noble-metal-based electrocatalysts (Figure 3c,d, Tables S2, and S3, Supporting Information) demonstrates that this sample belongs to the first-rate OER catalysts in both acid and alkaline electrolytes.

The stability issue is further evaluated with several approaches. First, the accelerated decay test result suggests that the curve after 1 and 5 k cycles shifted slightly to the positive direction than the initial one, and  $\eta_{10}$  merely increased from the initial

176 mV to the last 186 mV, as displayed in Figure 3a and Figure S22a, Supporting Information. Meanwhile, the gently increased charge transfer resistance ( $R_{ct}$ ) indicated from the Nyquist plots (Figure S22b, Supporting Information) hints at the robust and complete electrode/electrolyte interface during the strong polarization process.<sup>[33]</sup> The post-catalytic characterization (Figure S22c,d, Supporting Information) suggests the porous microsheet assembled with uniform and weeny Ru@V-RuO<sub>2</sub> can be almost inherited, explaining its flourishing electrochemical capacity and stability during the water oxidation process. Besides, the potential only increased by 20 mV after 15 h of electrolysis, supporting the above stability. For commercial RuO<sub>2</sub>, the oxidation current quickly decayed to zero after several cyclic voltammetry (CV) cycles (Figure S23, Supporting Information), suggesting its poor stability. Impressively, the Ru@V-RuO<sub>2</sub>/C HMS also showcases the exceptional activity ( $\eta_{10} = 191 \text{ mV}$ ,  $b = 52.1 \text{ mV dec}^{-1}$ ) in 0.05 M H<sub>2</sub>SO<sub>4</sub> among these prestigious electrocatalysts (See details in Figure S24 and Table S4, Supporting Information), such as a/c-RuO<sub>2</sub> ( $\eta_{10} = 205 \text{ mV}$ ,  $b = 48.6 \text{ mV dec}^{-1}$ ),<sup>[25]</sup> Ru@IrO<sub>x</sub> core–shell nanocrystal ( $\eta_{10} = 282 \text{ mV}$ ,  $b = 69.1 \text{ mV dec}^{-1}$ ),<sup>[16]</sup> Ru<sub>1</sub>-Pt<sub>3</sub>Cu<sub>1</sub> ( $\eta_{10} = 220 \text{ mV}$ ,  $b = 50.0 \text{ mV dec}^{-1}$ ),<sup>[34]</sup> along with the robust electrolysis endurance. Similarly, the catalytic stability in 1.0 M KOH is satisfactory, as  $\eta_{10}$  just increases by 4% (Figure S25a, Supporting Information), and the  $R_{ct}$  also varies with a modicum (Figure S25b, Supporting Information). Moreover, the entire microsheet can be well reserved, the single entity almost maintains its original configuration and size, and the Ru and RuO<sub>2</sub> can be well distinguished (Figure S25c,d, Supporting Information), favoring the material's practicability with the minimal decay ratio of potential (0.93% h<sup>-1</sup>, Figure S25e, Supporting Information) during the long-time running of 25 h. Besides, according to the XPS analysis (Figure S26, Supporting Information), a few hydrous Ru oxides was formed on the surfaces before and after CV cycles of the OER process, while the whole electronic structure of Ru is almost unchanged.<sup>[35,36]</sup>

Hydrogen evolution performance was then studied in acid and alkaline solutions. The linear sweep voltammetry curves (Figure 3e) obtained in 0.5 M H<sub>2</sub>SO<sub>4</sub> manifest that Ru@V-RuO<sub>2</sub>/C HMS possesses superior activity than that of the synthesized Ru/C HMS and commercial Pt/C (20 wt%). Specifically, the miniature  $\eta_{10}$  (47 mV, Figure S27a, Supporting Information) along with the Tafel slope value (55.1 mV dec<sup>-1</sup>, Inset in Figure 3e) of this sample locates in the competing level among the reported noble metal-based electrocatalysts in acid condition.<sup>[37–39]</sup> Furthermore, Ru@V-RuO<sub>2</sub>/C HMS exhibits the extraordinary activity in 1.0 M KOH (Figure 3f) with an ultrasmall  $\eta_{10}$  and Tafel slope value (45.1 mV dec<sup>-1</sup>, Inset in Figure 3f), superior to the benchmark Pt/C (33 mV, 53.4 mV dec<sup>-1</sup>) and Ru/C HMS (26 mV, 51.0 mV dec<sup>-1</sup>), also advantageous among the advanced Ru-based materials, such as Ru-Mo<sub>2</sub>C@CNT ( $\eta_{10} = 15 \text{ mV}$ ),<sup>[40]</sup> Ru@GnP ( $\eta_{10} = 22 \text{ mV}$ ),<sup>[41]</sup> Ru-NC-700 ( $\eta_{10} = 12 \text{ mV}$ ).<sup>[42]</sup> On the other hand, the almost unchanged polarization curves (Figure 3e,f) and  $\eta_{10}$  (Figure S27, Supporting Information) after 5k and 10k cycles in both acid and alkaline solutions point to the noteworthy electrochemical stability of this material for HER. Furthermore, the possible structural evolution of the post-catalytic sample dissected by TEM images and XRD (Figure S28, Supporting Information) exhibits the nanoparticle-composited sheet with the mixed phases of Ru and RuO<sub>2</sub>,

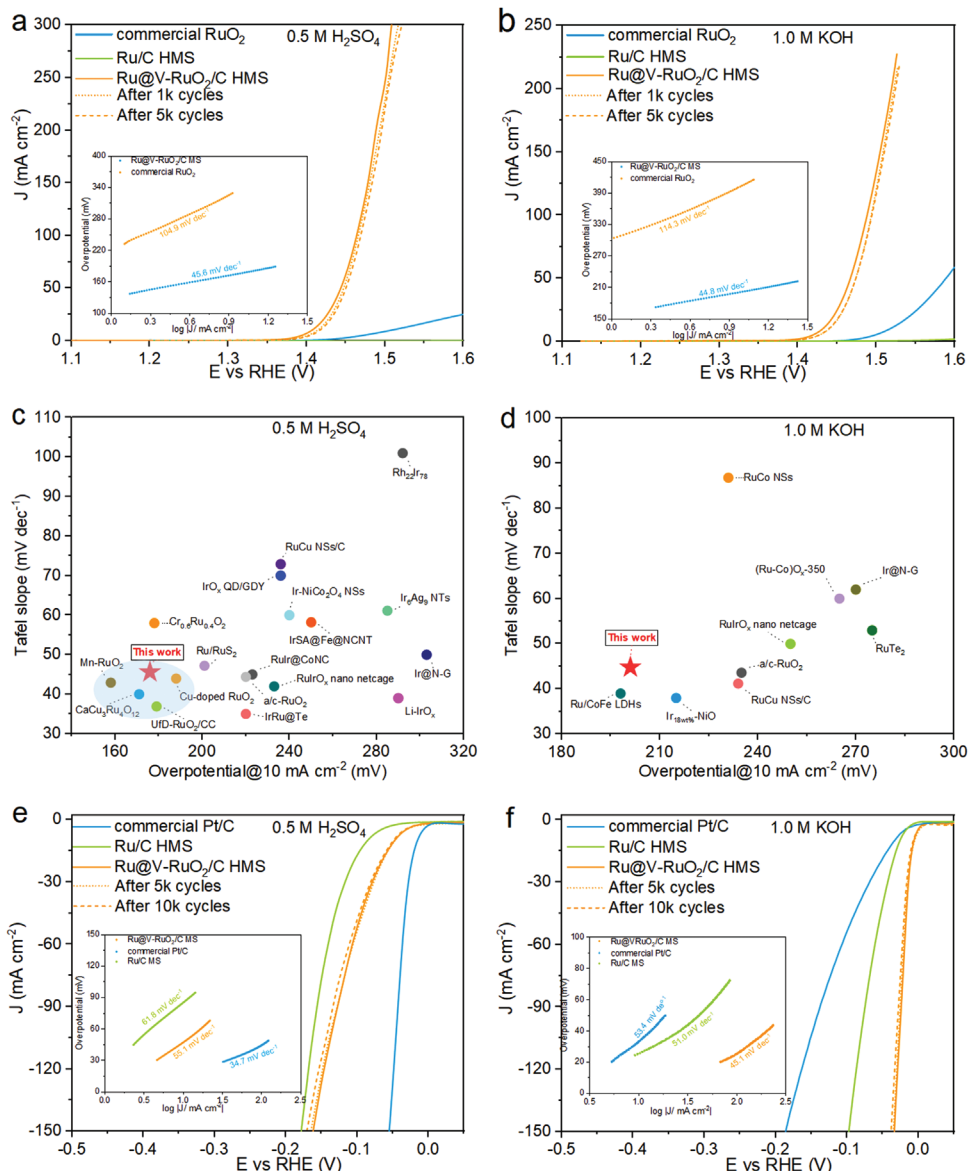


**Figure 3.** The electrochemical studies of catalysts in different electrolytes. a) OER polarization curves of commercial  $\text{RuO}_2$ ,  $\text{Ru/C HMS}$ ,  $\text{Ru@V-RuO}_2/\text{C HMS}$  as well as its subsequent curves during different cycles in 0.5 M  $\text{H}_2\text{SO}_4$  and b) 1.0 M KOH; c,d) comparison of overpotentials at 10  $\text{mA cm}^{-2}$  and Tafel slopes for  $\text{Ru@V-RuO}_2/\text{C HMS}$  with these excellent noble metal-based OER catalysts in 0.5 M  $\text{H}_2\text{SO}_4$  (c) and 1.0 M KOH (d); e,f) HER polarization curves of  $\text{Pt/C}$ ,  $\text{Ru/C HMS}$ ,  $\text{Ru@V-RuO}_2/\text{C HMS}$ , and its subsequent curves during different cycles in 0.5 M  $\text{H}_2\text{SO}_4$  (e) and 1.0 M KOH (f); the insets in (a,b,e,f) show the corresponding Tafel slope plots.

suggesting the multiscale steadiness from the chemical composition to the monolithic framework. The unchanged chemical valence of Ru as well as the slight increase of OH on the surface shown in Figure S29, Supporting Information, support the stability of the sample during the HER process. Meaningfully,  $\text{Ru@V-RuO}_2/\text{C HMS}$  delivers better OER activity in acid conditions while the superior HER capacity in alkaline solution, thus is important to compensate for the mismatched OER and HER process, benefitting the more stable operation of overall water electrolysis in the pH-varied condition.

To trace the activity origin, the theoretical calculation has been utilized to establish the structure–activity relationship. The Ru

(001) surface,  $\text{RuO}_2$  (110) surface, and the heterostructure of Ru (001) with  $\text{RuO}_2$  (110) surface doped with O vacancies on the  $\text{RuO}_2$  (110) surface ( $\text{Ru@V-RuO}_2$ ) was utilized as the models for the subsequent calculations, as portrayed in Figures S30–S34, Supporting Information. According to the Bader charge analysis (Figure S35, Tables S6, and S7, Supporting Information), the oxidation valence of Ru in  $\text{RuO}_2$  (110) of the  $\text{Ru@V-RuO}_2$  is lower than the perfect  $\text{RuO}_2$ , consistent with the XAS and XPS analysis, supporting the rationality of this model. The hydrogen adsorption free energy ( $\Delta G_{\text{H}^*}$ ) can bridge the apparent kinetics behavior with the intrinsic activity, and the value closer to zero reflects the better catalytic capacity.<sup>[43]</sup> The free energy plots in

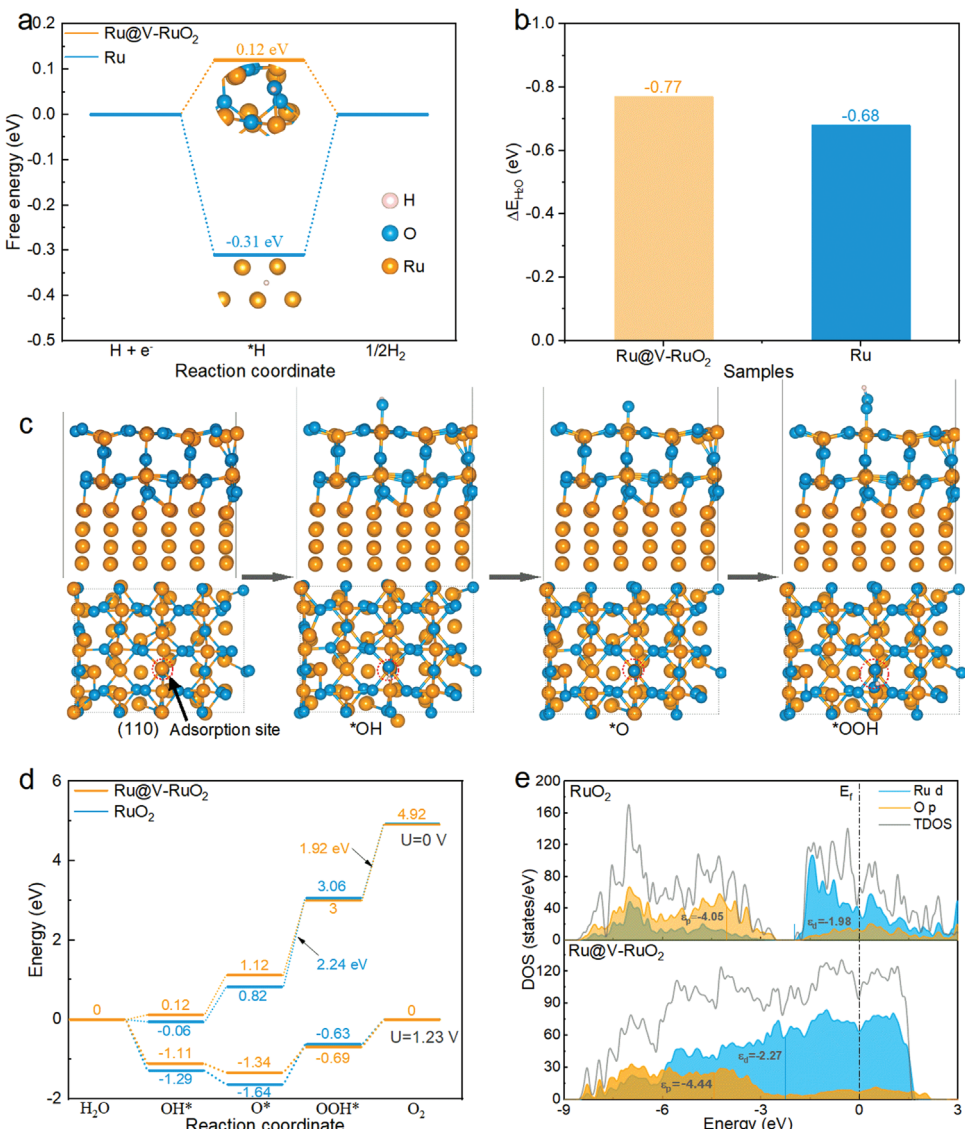


**Figure 4.** The theoretical understanding of HER/OER activity on Ru@V-RuO<sub>2</sub>. a) Free energy of H adsorption on the RuO<sub>2</sub> (110) surface in Ru@V-RuO<sub>2</sub> and (001) surface of Ru as well as the corresponding chemisorption models. b) Their water adsorption energy. c) OH, O, OOH intermediates adsorption configurations on the (110) surface of RuO<sub>2</sub> in Ru@V-RuO<sub>2</sub>. d) Free energy diagrams for OER on the RuO<sub>2</sub> (110) surface in RuO<sub>2</sub> and Ru@V-RuO<sub>2</sub>. e) The PDOSs projected on the p orbitals of O atoms for RuO<sub>2</sub> (top) and Ru@V-RuO<sub>2</sub> (bottom).

Figure 4a portray that the H adsorbed on Ru (001) plane (Figure S36a, Supporting Information) is too strong (-0.31 eV) for the follow-up desorption.<sup>[44]</sup> Meanwhile, the more thermoneutral H adsorption (0.12 eV) on the RuO<sub>2</sub> (110) plane of Ru@V-RuO<sub>2</sub> (Figure S36b, Supporting Information) means the accelerated desorption of hydrogen, explaining the better HER activity of Ru@V-RuO<sub>2</sub>/C HMS (47 mV@10 mA cm<sup>-2</sup>) than that of Ru/C HMS (85 mV@10 mA cm<sup>-2</sup>) experimentally. Further, the partial density of states (PDOSs, Figure S37, Supporting Information) projected on the d orbitals of Ru atoms for Ru@V-RuO<sub>2</sub> and Ru near the Fermi level are continuous and close, reflecting that arming the sub-nanometer skin of RuO<sub>2</sub> for the Ru core keeps the better conductivity to transfer the electron. Besides, the negative shift of the d-band center ( $\epsilon_d$ ) from Ru (-2.23 eV) to Ru@V-RuO<sub>2</sub> (-2.27 eV) leads to the weak adsorp-

tion strength, exploring its improved HER performance.<sup>[45]</sup> Furthermore, the more negative water adsorption energy ( $\Delta E_{H2O}$ ) presented in Figure 4b on the surface of Ru@V-RuO<sub>2</sub> (-0.77 eV, Figure S38a, Supporting Information) than that on Ru (-0.68 eV, Figure S38b, Supporting Information) is preferred for strong water molecule adsorption. Further, the negative of OH adsorption peak and the CO oxidation (Figure S39, Supporting Information) of Ru@V-RuO<sub>2</sub>/C HMS suggests its better ability of OH-adsorption, implying the dissociation of H<sub>2</sub>O is favorable.<sup>[46]</sup> Thus contribute to the macroscopically impressive HER activity of Ru@V-RuO<sub>2</sub>/C HMS (6 mV@10 mA cm<sup>-2</sup>) in alkaline condition.<sup>[47]</sup>

Next, the OER process was exerted on density functional theory (DFT) calculation to decipher the possible reason for the brilliant performance. It is usually accepted that the OER proceeds the

consecutive four-proton-coupled electron transfer steps involved with the intermediates of  $^*\text{OH}$ ,  $^*\text{O}$ , and  $^*\text{OOH}$ , as shown in Figure 4c and Figure S40, Supporting Information.<sup>[48]</sup> The free energy profiles mapped in Figure 4d can further discern the activity difference. At zero potential, all the four-step reactions during the OER for  $\text{RuO}_2$  and

$\text{Ru@V-RuO}_2$  moves uphill in free energy. As for  $\text{RuO}_2$ , the splitting of the second water to form  $^*\text{OOH}$  needs the largest free energy of 2.24 eV to make the oxygen evolution exothermic for  $\text{RuO}_2$ . At the equilibrium potential (1.23 V), the first two steps become spontaneous and the formation of  $^*\text{OOH}$  (the third step) needs to overcome the energy barrier of 1.01 eV to make the reaction occur, thus is the rate-determining step (RDS) in the OER. Differently, the RDS of  $\text{Ru@V-RuO}_2$  changes from the formation of  $^*\text{OOH}$  (the third step) to the release of  $\text{O}_2$  (the last step) with the decreased free energy (1.92 eV@0 V and 0.69 eV@1.23 V), which is agreed with the largely improved activity ( $\eta_{10}$  decreased by 101/86 mV in acid/alkaline solution than those of  $\text{RuO}_2$ ), denoting the importance of arming  $\text{RuO}_2$  sub-nanometer skin for inner Ru core to strengthen the materials' OER activity collaboratively. The PDOSSs of the Ru 4d and O 2p orbit were further investigated to dig out the deeper reason for the enhanced OER activity. As interpreted in Figure 4e, the negative shift of the d-band center from -1.98 eV of  $\text{RuO}_2$  to -2.09 eV of  $\text{Ru@V-RuO}_2$  as well as a smaller charge transfer (Figure S41, Supporting Information) from the  $\text{Ru@V-RuO}_2$  (0.62 e) to the  $^*\text{O}$  than that form  $\text{RuO}_2$  (0.64 e) results in the weaker chemical bond between the surface and the adsorbed oxygen-based species ( $^*\text{O}$ ), thus optimizing the adsorption free energy theoretically and reducing the overpotential experimentally. Besides, the more negative p-band center ( $\epsilon_p$ , -4.44 eV) of  $\text{Ru@V-RuO}_2$  than that of the  $\text{RuO}_2$  (-4.05 eV) discloses the low activity of lattice oxygen to participate in the oxidation reaction, so contributing to the enhanced structural robustness and exceptional electrochemical stability of  $\text{Ru@V-RuO}_2$  during the OER process.<sup>[49]</sup> Accordingly, clothing the Ru core with the functional  $\text{RuO}_2$  sub-nanometer armor is influential to activate the OER activity and prolong the longevity of Ru-based electrocatalysts.

To dig out the importance of  $\text{O}_v$ , the  $\text{Ru@V-RuO}_2$  models with different  $\text{O}_v$  content have been built, the  $\text{Ru@V-RuO}_2/\text{C}$  HMS has also been synthesized, which is displayed in Figures S42–S46, Supporting Information. As shown in Figure S42c, Supporting Information, the  $\text{Ru@V-RuO}_2$  with one  $\text{O}_v$  needs the overpotential of 0.86 eV to overcome the energy barrier from  $^*\text{O}$  to  $^*\text{OOH}$ , while the  $\text{Ru@V-RuO}_2$  with two  $\text{O}_v$  can transfer the RDS from  $^*\text{O} \rightarrow ^*\text{OOH}$  to  $^*\text{OOH} \rightarrow ^*\text{O}_2$  with the reduced overpotential of 0.69 eV. Experimentally, the  $\text{Ru@V-RuO}_2/\text{C}$  HMS (5 h) with the few  $\text{O}_v$  contents (spin concentration is  $2.527 \times 10^{11} \text{ mm}^{-3}$ ) has the worse OER activity (211 mV@10 mA cm $^{-2}$  in 1.0 M KOH and 194 mV@10 mA cm $^{-2}$  in 0.5 M H<sub>2</sub>SO<sub>4</sub>) than that for  $\text{Ru@V-RuO}_2/\text{C}$  HMS oxidized for 3 h (the highest spin concentration of  $3.41 \times 10^{12} \text{ mm}^{-3}$ ). Besides, the abundant  $\text{O}_v$  can make the hydrogen adsorption on the  $\text{RuO}_2$  (110) of  $\text{Ru@V-RuO}_2$  closer to the thermal-neutral level, consistent with the electrochemical results that the fewer  $\text{O}_v$  decorated  $\text{Ru@V-RuO}_2/\text{C}$  HMS (5 h) exhibits inferior HER activity than the  $\text{Ru@V-RuO}_2/\text{C}$  HMSs with rich  $\text{O}_v$  ( $2.725 \times 10^{12} \text{ mm}^{-3}$  for 1 h and  $3.41 \times 10^{12} \text{ mm}^{-3}$  for 3 h, Figure S45f–h, Supporting Information). Hence, the  $\text{O}_v$  content in the  $\text{Ru@V-RuO}_2$  is helpful to boost the HER

and OER activity. Further, the role of C in this hybrid was addressed via a series of experiments and calculations. Owing to the difficulty of obtaining  $\text{Ru@V-RuO}_2$  without C,  $\text{RuO}_2$  microsheet ( $\text{RuO}_2$  HMS, Figure S47, Supporting Information) without  $\text{O}_v$  and  $\text{RuO}_2/\text{C}$  HMS were compared to reflect the role of C in the  $\text{Ru@V-RuO}_2/\text{C}$  HMS indirectly. The  $\text{RuO}_2$  MS has inferior OER behavior than that of the carbon-base counterpart in the pH-wide condition (Figures S48, Supporting Information). Besides, its HER performance is superior to  $\text{RuO}_2$  MS (9 mV in 1.0 M KOH and 94 mV in 0.5 M H<sub>2</sub>SO<sub>4</sub> versus 20 mV in 1.0 M KOH and 95 mV in 0.5 M H<sub>2</sub>SO<sub>4</sub>, Figure S49, Supporting Information). This implies the coupling of  $\text{RuO}_2$  and C can improve reaction kinetics. On the other hand, the  $\text{RuO}_2/\text{C}$  HMS possesses the larger  $C_{dl}$  values in different electrolytes (Figure S50, Supporting Information), demonstrating the existence of carbon can provide abundant active sites. Then, the DFT calculation (Figure S51, Supporting Information) presents that the  $\text{RuO}_2/\text{C}$  hybrid displays a reduced energy barrier from  $^*\text{O}$  to  $^*\text{OOH}$  than the  $\text{RuO}_2$  counterpart (1.01 eV), supporting the superiority of  $\text{RuO}_2/\text{C}$  over  $\text{RuO}_2$  based on the ECSA-corrected polarization curve of them (Figure S52, Supporting Information). Hence, the coupling carbon is also helpful to improve the electrocatalytic performance of  $\text{Ru@V-RuO}_2/\text{C}$  HMS.

Besides the superiority of electronic structures coming from the core-shell  $\text{Ru@V-RuO}_2$  heterostructure, several geometric advantages are also critical to contributing to the wonderful electrocatalytic activity and stability of OER and HER. First, the 2D microsheet can fully expose the  $\text{Ru@V-RuO}_2$  surface; next, the abundant nanopores can accelerate the gas release and refresh the active sites quickly for the constant high-speed reaction; then, the coupled carbon matrix can offer the highway for electron transfer and maintains the whole structural stability; last but not the least, the ultrasmall nanoclusters can provide the rich active sites to improve the apparent reaction kinetics.

The splendid activity for OER and HER in the pH-wide range makes  $\text{Ru@V-RuO}_2/\text{C}$  HMS work as the universally compatible electrocatalysts to drive the overall water electrolysis. As demonstrated in Figure 5a,  $\text{Ru@V-RuO}_2/\text{C}$  HMS only needs the low voltages of 1.467 V in 0.5 M H<sub>2</sub>SO<sub>4</sub> and 1.437 V in 1.0 M KOH to reach 10 mA cm $^{-2}$ , almost classifying as the kinds of top-notch bifunctional noble-metal electrocatalysts (Figure 5b and Table S5, Supporting Information). Even in 0.05 M H<sub>2</sub>SO<sub>4</sub>, the  $\eta_{10}$  value is as low as 236 mV, also superior to the reported value.<sup>[50]</sup> Importantly, the catalyst can maintain stable electrolysis within 25 h in different electrolytes (Figure 5c), suggesting good durability. Besides, one AA battery can effortlessly power the two-electrode electrolyzer to release hydrogen and oxygen bubble gas over the entire pH range (0–14), as displayed in Figure 5d and Movies S1–S3, Supporting Information. The pH-wide activity and stability would improve the usability and buffering capacity of  $\text{Ru@V-RuO}_2/\text{C}$  HMS to overcome the main drawbacks of existing electrolysis technologies.<sup>[51]</sup>

### 3. Conclusions

We have precisely synthesized a kind of core-shell heterostructure by thermally controlled oxidation of the Ru/C hybrid microsheet to successfully arm the oxygen-vacancy-enriched  $\text{RuO}_2$

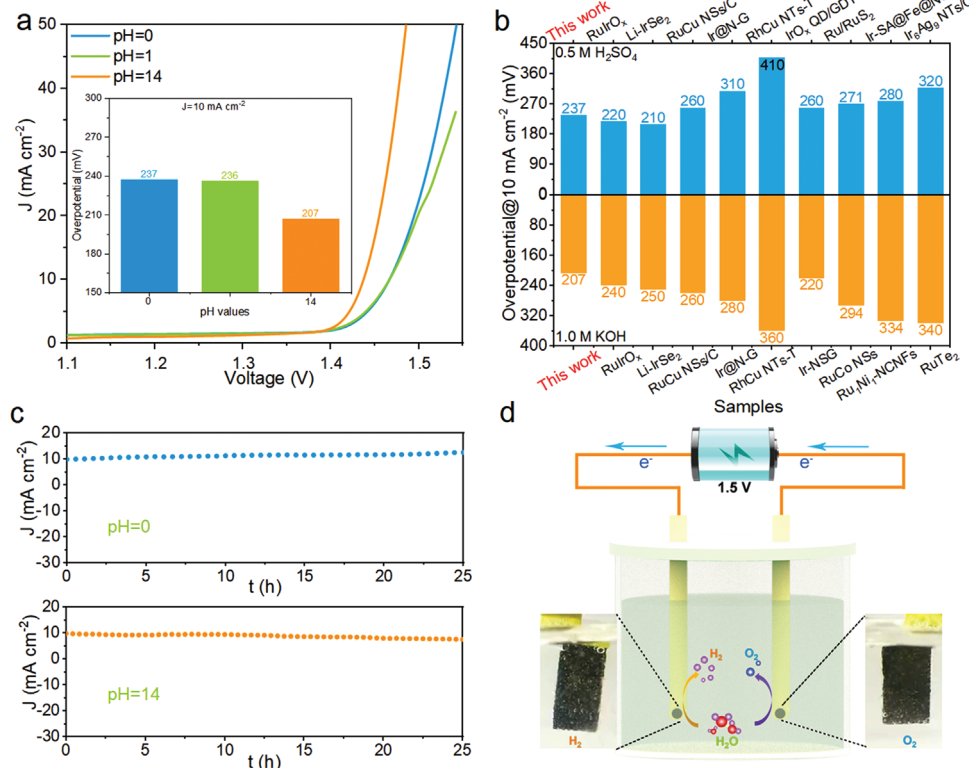


**Figure 5.** Overall water splitting study of Ru@V-RuO<sub>2</sub>/C HMS||Ru@V-RuO<sub>2</sub>/C HMS. a) Polarization curves, inset shows  $\eta_{10}$  values; b) comparison of  $\eta_{10}$  values of Ru@V-RuO<sub>2</sub>/C HMS with the reported catalysts under acid (top) and alkaline (bottom) solution; c) time-dependent current density curves at 1.47 V in 0.5 M H<sub>2</sub>SO<sub>4</sub> and 1.44 V in 1.0 M KOH; d) schematic diagram of 1.5 V-battery-driven OWS system and the optical photos of generated bubble gas in anode and cathode.

sub-nanometer skin on the Ru core (Ru@V-RuO<sub>2</sub>/C HMS). Owning to modulated interfacial electronic structure and the strain effect induced by the core–shell heterostructure, as well as the large specific surface area, the abundant pores, the better conductivity, and anticorrosion ability, the obtained Ru@V-RuO<sub>2</sub>/C HMS can be assigned to the kind of top-notch bifunctional electrocatalysts toward HER and OER in the pH-wide condition. Numerically, the Ru@V-RuO<sub>2</sub>/C HMS merely needs the ultrasmall overpotentials of 176/201 mV for OER and 46/6 mV toward HER to reach 10 mA cm<sup>-2</sup> in 0.5 M H<sub>2</sub>SO<sub>4</sub>/1.0 M KOH, respectively. DFT calculations decipher that the arming of the O<sub>v</sub>-rich RuO<sub>2</sub> sub-nanometer skin to the Ru core can steer the d/p band center of Ru and O, thus balancing the adsorption/desorption H behavior ( $\Delta G_{H^*} = 0.13$  eV) for accelerating the HER kinetics, also weakening the adsorption of oxygen-based intermediates for reforming OER process. Impressively, the small applied voltages of less than 1.5 V (1.467 V in 0.5 M H<sub>2</sub>SO<sub>4</sub> and 1.437 V in 1.0 M KOH, respectively) can be achieved to afford 10 mA cm<sup>-2</sup> in the two-electrode water electrolysis system, underpinning the significance of arming the Ru core with the RuO<sub>2</sub> sub-nanometer skin to reach the satisfactory bifunctionality toward HER and OER. Our work may provide some guidelines on the design of high-efficient electrocatalysts via atomic-scale controllable decoration of the functional armor on the active core.

## Supporting Information

Supporting Information is available from the Wiley Online Library or from the author.

## Acknowledgements

Y.L. and W.W. contributed equally to this work. G.Z. acknowledges the financial support from the National Key R&D Program of China (2022YFA1504001), National Natural Science Foundation of China (Grant No. 52072359), the Recruitment Program of Global Experts, and the Fundamental Research Funds for the Central Universities (WK 2060000016). The numerical calculations in this paper were done at the Supercomputing Center at the University of Science and Technology of China and TianHe-2 at LvLiang Cloud Computing Center of China. The XAS characterizations of O K edge and XPS depth profile were performed at beamline BL10B in NSRL, China. The XAS characterizations of Ru K edge were collected on the beamline BL01C1 in NSRRC, China.

## Conflict of Interest

The authors declare no conflict of interest.

## Data Availability Statement

The data that support the findings of this study are available from the corresponding author upon reasonable request.

## Keywords

bifunctionality, core–shell structures, oxygen vacancies, sub-nanometer skin, water splitting

Received: July 13, 2022

Revised: November 21, 2022

Published online: April 28, 2023

- [1] M. Zhang, J. Gong, The Evolvement of China-EU Cooperationon Climate Change and its New Opportunities under the European Green Deal, **2020**.
- [2] T. E. Mallouk, *Nat. Chem.* **2013**, *5*, 362.
- [3] J. A. Turner, *Science* **2004**, *305*, 972.
- [4] S. Li, B. Chen, Y. Wang, M. Y. Ye, P. A. van Aken, C. Cheng, A. Thomas, *Nat. Mater.* **2021**, *20*, 1240.
- [5] S. L. Jiao, X. W. Fu, S. Y. Wang, Y. Zhao, *Environ. Sci.* **2021**, *14*, 1722.
- [6] Y. Zhu, J. Zhang, Q. Qian, Y. Li, Z. Li, Y. Liu, C. Xiao, G. Zhang, Y. Xie, *Angew. Chem., Int. Ed.* **2022**, *61*, e202113082.
- [7] F. Song, X. Hu, *Nat. Commun.* **2014**, *5*, 4477.
- [8] B. Zhang, X. Zheng, O. Voznyy, R. Comin, M. Bajdich, M. Garcia-Melchor, L. Han, J. Xu, M. Liu, L. Zheng, F. P. Garcia de Arquer, C. T. Dinh, F. Fan, M. Yuan, E. Yassitepe, N. Chen, T. Regier, P. Liu, Y. Li, P. De Luna, A. Janmohamed, H. L. Xin, H. Yang, A. Vojvodic, E. H. Sargent, *Science* **2016**, *352*, 333.
- [9] Q. Qian, Y. Li, Y. Liu, L. Yu, G. Zhang, *Adv. Mater.* **2019**, *31*, 1901139.
- [10] R. Subbaraman, D. Tripkovic, D. Strmcnik, K. C. Chang, M. Uchimura, A. P. Paulikas, V. Stamenkovic, N. M. Markovic, *Science* **2011**, *334*, 1256.
- [11] T. Zheng, C. Shang, Z. He, X. Wang, C. Cao, H. Li, R. Si, B. Pan, S. Zhou, J. Zeng, *Angew. Chem., Int. Ed.* **2019**, *58*, 14764.
- [12] Y. Li, J. Zhang, Y. Liu, Q. Qian, Z. Li, Y. Zhu, G. Zhang, *Sci. Adv.* **2020**, *6*, eabb4197.
- [13] J. Mahmood, F. Li, S. M. Jung, M. S. Okyay, I. Ahmad, S. J. Kim, N. Park, H. Y. Jeong, J. B. Baek, *Nat. Nanotechnol.* **2017**, *12*, 441.
- [14] M. Li, Z. Zhao, T. Cheng, A. Fortunelli, C. Y. Chen, R. Yu, Q. Zhang, L. Gu, B. V. Merinov, Z. Lin, E. Zhu, T. Yu, Q. Jia, J. Guo, L. Zhang, W. A. Goddard, 3rd, Y. Huang, X. Duan, *Science* **2016**, *354*, 1414.
- [15] J. N. Schwämmlein, B. M. Stühmeier, K. Wagenbauer, H. Dietz, V. Tileli, H. A. Gasteiger, H. A. El-Sayed, *J. Electrochem. Soc.* **2018**, *165*, H229.
- [16] J. Q. Shan, C. X. Guo, Y. H. Zhu, S. M. Chen, L. Song, M. Jaroniec, Y. Zheng, S. Z. Qiao, *Chem* **2019**, *5*, 445.
- [17] M. Li, Z. Zhao, Z. Xia, M. Luo, Q. Zhang, Y. Qin, L. Tao, K. Yin, Y. Chao, L. Gu, W. Yang, Y. Yu, G. Lu, S. Guo, *Angew. Chem., Int. Ed.* **2021**, *60*, 8243.
- [18] J. K. Gao, J. P. Wang, X. F. Qian, Y. Y. Dong, H. Xu, R. J. Song, C. F. Yan, H. C. Zhu, Q. W. Zhong, G. D. Qian, J. M. Yao, *J. Solid State Chem.* **2015**, *228*, 60.
- [19] Q. Wang, S. Chen, F. Shi, K. Chen, Y. Nie, Y. Wang, R. Wu, J. Li, Y. Zhang, W. Ding, Y. Li, L. Li, Z. Wei, *Adv. Mater.* **2016**, *28*, 10673.
- [20] X. Cui, P. Ren, C. Ma, J. Zhao, R. Chen, S. Chen, N. P. Rajan, H. Li, L. Yu, Z. Tian, D. Deng, *Adv. Mater.* **2020**, *32*, 1908126.
- [21] P. Strasser, S. Koh, T. Anniyev, J. Greeley, K. More, C. Yu, Z. Liu, S. Kaya, D. Nordlund, H. Ogasawara, M. F. Toney, A. Nilsson, *Nat. Chem.* **2010**, *2*, 454.
- [22] L. Gan, R. Yu, J. Luo, Z. Cheng, J. Zhu, *J. Phys. Chem. Lett.* **2012**, *3*, 934.
- [23] L. Bu, N. Zhang, S. Guo, X. Zhang, J. Li, J. Yao, T. Wu, G. Lu, J. Y. Ma, D. Su, X. Huang, *Science* **2016**, *354*, 1410.
- [24] Y. Sun, K. Xu, Z. Wei, H. Li, T. Zhang, X. Li, W. Cai, J. Ma, H. J. Fan, Y. Li, *Adv. Mater.* **2018**, *30*, 1802121.
- [25] L. Zhang, H. Jang, H. Liu, M. G. Kim, D. Yang, S. Liu, X. Liu, J. Cho, *Angew. Chem., Int. Ed.* **2021**, *60*, 18821.
- [26] Y. G. Li, Y. Wang, J. M. Lu, B. Yang, X. Y. San, Z. S. Wu, *Nano Energy* **2020**, *78*, 105185.
- [27] D. J. Morgan, *Surf. Interface Anal.* **2015**, *47*, 1072.
- [28] N. Wang, S. Ning, X. Yu, D. Chen, Z. Li, J. Xu, H. Meng, D. Zhao, L. Li, Q. Liu, B. Lu, S. Chen, *Appl. Catal., B* **2022**, *302*, 120838.
- [29] Y. Tian, S. Wang, E. Velasco, Y. Yang, L. Cao, L. Zhang, X. Li, Y. Lin, Q. Zhang, L. Chen, *iScience* **2020**, *23*, 100756.
- [30] J. Zhou, J. Wang, H. Fang, C. Wu, J. N. Cutler, T. K. Sham, *Chem. Commun.* **2010**, *46*, 2778.
- [31] X. Miao, L. Zhang, L. Wu, Z. Hu, L. Shi, S. Zhou, *Nat. Commun.* **2019**, *10*, 3809.
- [32] T. Reier, M. Oezaslan, P. Strasser, *ACS Catal.* **2012**, *2*, 1765.
- [33] Y. Li, J. Li, Q. Qian, X. Jin, Y. Liu, Z. Li, Y. Zhu, Y. Guo, G. Zhang, *Small* **2021**, *17*, 2008148.
- [34] Y. C. Yao, S. L. Hu, W. X. Chen, Z. Q. Huang, W. C. Wei, T. Yao, R. R. Liu, K. T. Zang, X. Q. Wang, G. Wu, W. J. Yuan, T. W. Yuan, B. Q. Zhu, W. Liu, Z. J. Li, D. S. He, Z. G. Xue, Y. Wang, X. S. Zheng, J. C. Dong, C. R. Chang, Y. X. Chen, X. Hong, J. Luo, S. Q. Wei, W. X. Li, P. Strasser, Y. E. Wu, Y. D. Li, *Nat. Catal.* **2019**, *2*, 304.
- [35] Y. Dang, T. Wu, H. Tan, J. Wang, C. Cui, P. Kerns, W. Zhao, L. Posada, L. Wen, S. L. Suib, *Energy Environ. Sci.* **2021**, *14*, 5433.
- [36] Q. Liang, A. Bieberle-Hütter, G. Brocks, *J. Phys. Chem.* **2022**, *126*, 1337.
- [37] D. Liu, X. Li, S. Chen, H. Yan, C. Wang, C. Wu, Y. A. Haleem, S. Duan, J. Lu, B. Ge, P. M. Ajayan, Y. Luo, J. Jiang, L. Song, *Nat. Energy* **2019**, *4*, 512.
- [38] W. Zhong, B. Xiao, Z. Lin, Z. Wang, L. Huang, S. Shen, Q. Zhang, L. Gu, *Adv. Mater.* **2021**, *33*, 2007894.
- [39] Y. Liu, X. Li, Q. Zhang, W. Li, Y. Xie, H. Liu, L. Shang, Z. Liu, Z. Chen, L. Gu, Z. Tang, T. Zhang, S. Lu, *Angew. Chem., Int. Ed.* **2020**, *59*, 1718.
- [40] X. Wu, Z. Wang, D. Zhang, Y. Qin, M. Wang, Y. Han, T. Zhan, B. Yang, S. Li, J. Lai, L. Wang, *Nat. Commun.* **2021**, *12*, 4018.
- [41] F. Li, G. F. Han, H. J. Noh, I. Ahmad, I. Y. Jeon, J. B. Baek, *Adv. Mater.* **2018**, *30*, 1803676.
- [42] B. Lu, L. Guo, F. Wu, Y. Peng, J. E. Lu, T. J. Smart, N. Wang, Y. Z. Finrock, D. Morris, P. Zhang, N. Li, P. Gao, Y. Ping, S. Chen, *Nat. Commun.* **2019**, *10*, 631.
- [43] J. Greeley, T. F. Jaramillo, J. Bonde, I. B. Chorkendorff, J. K. Norskov, *Nat. Mater.* **2006**, *5*, 909.
- [44] Q. Qian, J. Zhang, J. Li, Y. Li, X. Jin, Y. Zhu, Y. Liu, Z. Li, A. El-Harairy, C. Xiao, G. Zhang, Y. Xie, *Angew. Chem., Int. Ed.* **2021**, *60*, 5984.
- [45] J. Cai, Y. Song, Y. Zang, S. Niu, Y. Wu, Y. Xie, X. Zheng, Y. Liu, Y. Lin, X. Liu, G. Wang, Y. Qian, *Sci. Adv.* **2020**, *6*, eaaw8113.
- [46] J. Zhang, G. Chen, Q. Liu, C. Fan, D. Sun, Y. Tang, H. Sun, X. Feng, *Angew. Chem., Int. Ed.* **2022**, *61*, e202209486.
- [47] Y. Liu, J. Zhang, Y. Li, Q. Qian, Z. Li, Y. Zhu, G. Zhang, *Nat. Commun.* **2020**, *11*, 1853.
- [48] I. C. Man, H. Y. Su, F. Calle-Vallejo, H. A. Hansen, J. I. Martinez, N. G. Inoglu, J. Kitchin, T. F. Jaramillo, J. K. Norskov, J. Rossmeisl, *Chem-CatChem* **2011**, *3*, 1159.
- [49] Y. Shao, X. Xiao, Y. P. Zhu, T. Y. Ma, *Angew. Chem., Int. Ed.* **2019**, *58*, 14599.
- [50] Q. Wang, C. Q. Xu, W. Liu, S. F. Hung, H. Bin Yang, J. Gao, W. Cai, H. M. Chen, J. Li, B. Liu, *Nat. Commun.* **2020**, *11*, 4246.
- [51] Z. Zhuang, Y. Wang, C. Q. Xu, S. Liu, C. Chen, Q. Peng, Z. Zhuang, H. Xiao, Y. Pan, S. Lu, R. Yu, W. C. Cheong, X. Cao, K. Wu, K. Sun, Y. Wang, D. Wang, J. Li, Y. Li, *Nat. Commun.* **2019**, *10*, 4875.